# Effect of Porogen Molecular Architecture and Loading on Structure of Porous Thin Films

Hae-Jeong Lee, Christopher L. Soles,* Bryan D. Vogt,† Da-Wei Liu, Wen-li Wu, and Eric K. Lin

*Polymers Division, National Institute of Standards and Technology, Gaithersburg, Maryland 20899*

Ho-Cheol Kim, Victor Y. Lee, Willi Volksen, and Robert D. Miller

*IBM Research Division, Almaden Research Center, 650 Harry Road, San Jose, California 95120*

*Received March 26, 2008. Revised Manuscript Received September 30, 2008*

The effects of molecular architecture and loading of a porogen material on the structural characteristics of methylsilsesquioxane (MSQ)-based porous films are examined using X-ray porosimetry (XRP) and small-angle neutron scattering (SANS). Either linear (NG) or star-shaped (TP) polymers are used as the porogen here and blended with the MSQ material at loadings from 20 to 50% by mass, resulting in porosities between 30 and 60% by volume, regardless of porogen architecture. This indicates that the MSQ matrix material contains approximately 10% by volume inherent microporosity. The average pore size increases with increased porogen loadings in a way that depends on the porogen architecture. The NG porogen tends to aggregate, more than tripling the average pore size as the porogen loading increases from 20 to 50% by mass (22 to 76 Å in diameter). By contrast, the TP porogen has less propensity to aggregate, leading to a smaller increase in terms of percent change in the average pore size for the same porogen loading range (76 to 132 Å in diameter). Changes in the porogen type or loading do not influence the wall density (1.47 ± 0.01) g/cm$^3$ of the material between the pores, whereas the coefficient of thermal expansion (CTE) is approximately 1.5 times greater for the NG samples than for the TP samples at all porogen loadings.

## Introduction

Porous materials have potential in applications such as catalysts,[1] membranes,[2] chemical sensors,[3] optical application,[4] low dielectric constant (low-*k*) insulators,[5−13] and applications in biotechnology.[14,15] However, each application requires different pore dimensions and morphologies to achieve optimal performance. For catalytic and filtration applications, materials with interconnected macro- and mesopores exhibit enhanced device performance compared to monodispersed nanopores due to better mass transport through the multiscale pore network while maintaining high surface area on the level of the nanoporous system.[4] Conversely, low-*k* insulator materials with uniformly distributed and isolated (not interconnected) small pores are necessary to improve the properties essential to integrated circuit performance such as the mechanical strength, electrical properties, and limiting Cu diffusion through the insulator.[16]

Over the past several decades, extensive efforts have been devoted to developing porous materials. A diverse range of processing routes such as catalyzed sol−gel polymerization of surfactants or block copolymers,[17] selective degradation of material with UV exposure,[18] pyrolysis,[9] and selective

---

* To whom correspondence should be addressed. E-mail: csoles@nist.gov.
† Present address: Department of Chemical Engineering, Arizona State University, Tempe, AZ 85284.

(1) Jaroniec, M.; Choma, J.; Gorka, J.; Zawislak, A. *Chem. Mater.* **2008**, *20*, 1069.
(2) Valle, K.; Belleville, P.; Pereira, F.; Sanchez, C. *Nat. Mater.* **2006**, *5*, 107.
(3) Bao, Z. H.; Weatherspoon, M. R.; Shian, S.; Cai, Y.; Graham, P. D.; Allan, S. M.; Ahmad, G.; Dickerson, M. B.; Church, B. C.; Kang, Z. T.; Abernathy, H. W.; Summers, C. J.; Liu, M. L.; Sandhage, K. H. *Nature* **2007**, *446*, 172.
(4) Scott, B. J; Wirnsberger, G.; Stucky, G. D. *Chem. Mater.* **2001**, *13*, 3140.
(5) Hawker, C. J.; Hedrick, J. L.; Miller, R. D.; Volksen, W. *Mater. Res. Soc. Bull.* **2000**, *25*, 54.
(6) Kondoh, E.; Asano, T.; Nakashima, A.; Komatu, M. *J. Vac. Sci. Technol. B* **2000**, *18*, 1276.
(7) Mikoshiba, S.; Hayase, S. *J. Mater. Chem.* **1999**, *9*, 591.
(8) Ro, H. W.; Char, K.; Jeon, E.; Kim, H.-J.; Kwon, D.; Lee, H. J.; Lee, J.-K.; Rhee, H.-W.; Soles, C. L.; Yoon, D. Y. *Adv. Mater.* **2007**, *19*, 705.
(9) Yang, S.; Mirau, P.; Pai, C. S.; Nalamasu, O.; Reichmanis, E.; Lin, E. K.; Lee, H. J.; Gidley, D. W.; Sun, J. N. *Chem. Mater.* **2001**, *13*, 2762.
(10) Grill, A. *J. Appl. Phys.* **2003**, *93*, 1785.
(11) Huang, Q. R.; Volksen, W.; Huang, E.; Toney, M. C.; Frank, W.; Miller, R. D. *Chem. Mater.* **2002**, *14*, 3676.
(12) Si, J. J.; Ono, H.; Uchida, K.; Nozaki, S.; Morisaki, H.; Itoh, N. *Appl. Phys. Lett.* **2001**, *79*, 3140.
(13) Wang, Z.; Mitra, A.; Wang, H.; Huang, L.; Yan, Y. *Adv. Mater.* **2001**, *13*, 1463.
(14) Kim, H. C.; Kreller, C. R.; Tran, K. A.; Sisodiya, V.; Angelos, S.; Wallraff, G.; Swanson, S.; Miller, R. D. *Chem. Mater.* **2004**, *16*, 4267.
(15) Pirrung, M. C. *Angew. Chem., Int. Ed.* **2002**, *41*, 1276.
(16) Mosig, M.; Jacobs, T.; Brennan, K.; Rasco, M.; Wolf, J.; Augur, R. *Microelectron. Eng.* **2002**, *64*, 11.
(17) Huo, Q. S.; Margolese, D. I.; Ciesla, U.; Feng, P. Y.; Gier, T. E.; Sieger, P.; Leon, R.; Petroff, P. M.; Schuth, F.; Stucky, G. D. *Nature* **1994**, *368*, 317.
(18) Thurn-Albrecht, T.; Schotter, J.; Kästle, G. A.; Emley, N.; Shibauchi, T.; Krusin-Elbaum, L.; Guarini, K.; Black, C. T.; Tuominen, M. T.; Russell, T. P. *Science* **2000**, *290*, 2126.

10.1021/cm800872b CCC: $40.75 © 2008 American Chemical Society
Published on Web 11/26/2008

removal of low molar mass amphiphiles from hierarchically self-assembled polymeric supramolecules[19] have been employed to develop porous materials. One simple and facile route to generate pores in thin films is through use of sacrificial organic polymers (denoted as a porogen or pore-generator) dispersed within a matrix containing the precursor to the final material. Generally, the miscibility of the polymer with the precursor is poor, leading to phase separation of the polymer whose domains then define the pore. Pores are generated by volatilizing the sacrificial organic polymers at high temperature. The size, distribution, and morphology of the pores generated by this method depend strongly on the interaction between the matrix and porogens, composition of the hybrid blend, and the molecular architecture of porogens.[20]

One of the most common matrix materials for these sacrificial porogens is methylsilsesquioxane (MSQ). The MSQ oligomers change from amphiphilic to hydrophobic during the hydrolysis reaction at elevated temperature. This change in the physicochemical nature of the material alters the miscibility of the porogen that is initially dispersed in the MSQ-based oligomer precursor.[9,21] The evolving phase behavior of these blends combined with the changes in the local chain mobility during the vitrification reaction defines the final pore structure of these materials, thus providing a mechanism to control the material properties. However, characterizing subtle changes in the pore structure in these thin films to determine the process-structure−property relations for these materials remains a significant challenge.

One method to determine the detailed structure of porous thin films is X-ray porosimetry (XRP), which utilizes specular X-ray reflectivity (SXR) to quantify the uptake of the probe molecules inside the pores as the partial pressure of an adsorbate is varied.[22,23] The uptake of the organic probe molecules are measured directly from the change in the electron density of the film upon condensation within the film pores. In this work, we use XRP to study the influence of the molecular structure and loading of the porogen on the pore structures in two model systems. Two architecturally distinct porogens are used: thermally labile linear (NG) and star-shaped (TP) polymers. The porosity is controlled by increasing the porogen loading up to 50% by mass for each porogen. The effects of porogen architecture and loading on the pore size distribution (PSD), wall density, average film density, average pore size, pore connectivity, and coefficient of thermal expansion (CTE) will be discussed.

## Experimental Section

Certain commercial equipment and materials are identified in this paper in order to specify adequately the experimental procedure. In no case does such identification imply recommendation by the National Institute of Standards and Technology nor does it imply that the material or equipment identified is necessarily the best available for this purpose.

A copolymer of methyl trimethoxy silane and tetraethoxy silane with an approximate molecular mass of 2,000 g/mol was used as the oligomeric MSQ precursor in this study. A polyether polyol (6000 g/mol, Acclaim Polyol from Bayer) and a star polymer having amphiphilic arms were used as the NG and TP porogen, respectively. Synthesis of the TP porogen was described previously.[20] The porogens were dissolved in 1-methoxy-2-propanol acetate (PMAc) and mixed with MSQ precursor solution in propylene glycol propyl ether (PGPE). Thin films were prepared by spin-casting the solutions onto silicon wafers that were cleaned with a UV/ozone cleaner (UV-300H, SAMCO Inc.) at 100 °C. After spin casting, the wafers were heated to 450 °C at the rate of 5 °C/min. and the temperature was held constant for 2 h under nitrogen to simultaneously cross-link the MSQ precursor and decompose the porogens. After cross-linking, the surface morphology was characterized by atomic force microscopy (AFM, Dimension 3100, Digital Instruments) in tapping mode with standard silicon cantilevers (OTESPA from Veeco probes).

SXR measurements were performed using a modified high-resolution X-ray diffractometer in a $\theta-2\theta$ configuration at the specular condition, where the incident angle is equal to the detector angle, utilizing finely focused Cu-$K_\alpha$ radiation with a wavelength, $\lambda$, of 1.54 Å. The incident and reflected beams were conditioned with a four-bounce germanium (220) monochromator and a three-bounce germanium (220) channel cut crystal, respectively. The reflected intensity was collected as a function of the grazing incident angle over an angular range of 0.1−1.0° with an angular reproducibility of ±0.0001°.[24]

For the XRP measurements, toluene vapor was utilized as the absorbate probe molecule. SXR measurements monitor the changes in the critical angle for total external X-ray reflectance as a function of partial pressure. Changes in electron density of the film during the adsorption/desorption of toluene result in a shift of the critical angle, thus enabling a direct measure of the toluene present in the porous film. Films were first conditioned at 175 °C in vacuum (approximately $1.33 \times 10^{-3}$ torr) for 2 h to remove possible contaminants before conducting the measurements. The reference reflectivity of the film was taken at 25 °C under a flow 500 standard cubic centimeters per minute (sccm) of dry air. The toluene partial pressure was controlled by mixing streams of air saturated with toluene vapor and dry air using mass flow controllers. The total flow rate of two gas streams was fixed at 500 sccm, whereas the temperature was held at 25 °C to avoid the effects of temperature variation on the condensation of probe gases. After each change in partial pressure, 30 min was allowed for equilibration prior to reflectivity data collection. The PSD is estimated from the mass uptake as a function of partial pressure during adsorption and desorption cycles by applying the Kelvin equation.

An important property for microelectronics applications is the coefficient of thermal expansion (CTE) of the porous film. SXR can also quantify the CTE by measuring the film thickness as a function of temperature. Initially, the samples were annealed at 175 °C for 1 h under a vacuum to remove the potential contaminants. SXR measurements were then performed at 25, 75, 125, and 175 °C incrementally with 1 h allowed between temperatures for equilibration. Lastly, sample thickness after cooling back to 25 °C was measured to compare to the initial sample thickness in order

---

(19) Maki-Ontto, R.; de Moel, K.; de Odorico, W. *Adv. Mater.* **2001**, *13*, 117.

(20) Kim, H. C.; Wallraff, G.; Kreller, C. R.; Angelos, S.; Lee, V. Y.; Volksen, W.; Miller, R. D. *Nano Lett.* **2004**, *4*, 1169.

(21) Alexandridis, P.; Holzwarth, J. F.; Hatton, T. A. *Macromolecules* **1994**, *27*, 2414.

(22) Lee, H. J.; Soles, C. L.; Liu, D.; Bauer, B. J.; Wu, W. L. *J. Polym. Sci.: Part B: Polym. Phys.* **2002**, *40*, 2170.

(23) Lee, H. J.; Lin, E. K.; Bauer, B. J.; Wu, W. L.; Hwang, B. K.; Gray, W. D. *Appl. Phys. Lett.* **2003**, *82*, 1084.

(24) The data throughout the manuscript and in the figures are presented along with the standard uncertainty (±) involved in the measurement.

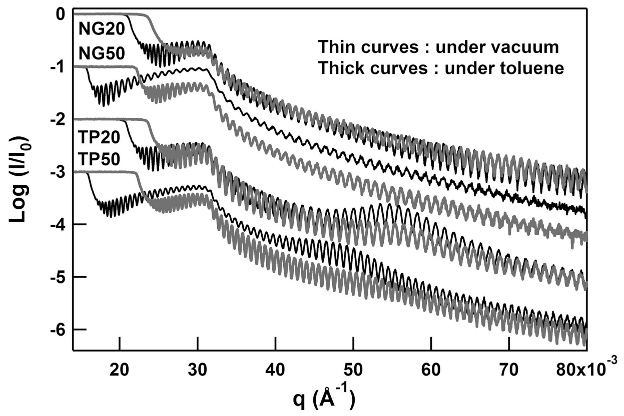

**Figure 1.** SXR curves of MSQ-based porous thin films prepared using linear (NG) and star shaped (TP) porogen with varying porogen loading. In the label for the reflectivity curves, first two letters denote molecular architecture of porogen and last two digits denote porogen loading contents. Those are presented as the logarithm of the ratio of the reflected beam intensity ($I$) to the incident beam intensity ($I_0$) versus the magnitude of the momentum transfer in the film thickness direction ($q$). The thin black and thick gray curves indicate the experimental data taken under vacuum and in the saturated toluene atmosphere, respectively. Curves are offset for the clarity.

to detect possible mass loss or pore collapse during the CTE measurement process.

Complementary small-angle neutron scattering (SANS) measurements were performed on the NG1 8 m SANS instrument at the NIST Center for Neutron Research utilizing a neutron wavelength of 6 Å with a wavelength spread (fwhm) of $\Delta\lambda/\lambda \approx 0.14$. The sample to detector distance was 3.6 m with the detector offset by 3.5° from the incident beam to increase the range of observable angles. Two-dimensional scattering patterns of the porous films were collected for up to 6 h to obtain sufficient statistics from a stack of 10 films oriented perpendicular to the incident beam. The circularly averaged two-dimensional data were corrected and reduced using standard methods.[25]

## Results and Discussion

SXR curve corresponding to the porous films from the two different porogen architectures, NG and TP, are shown in Figure 1. At small incident angles or small $q$ ($q = (4\pi/\lambda)\sin\theta$; where $\theta$ is the grazing incident angle of the X-ray beam), total external reflection of the beam occurs until the angle exceeds a critical value, corresponding to critical wave vector, $q_c$, where the incident X-rays begin to penetrate the films. At $q_c$, there is a sharp drop in the reflected intensity due to absorption as X-rays pass through the porous film and are then reflected by the silicon substrate. A second critical wave vector corresponding to the silicon substrate occurs at larger $q$; $q_{c,\text{silicon}} \approx 0.032$ Å$^{-1}$. A least-squares fitting routine based on the algorithm of Parratt[26] is used to accurately determine $q_c$ of the films. The critical wave vector is related to the density of the film through $q_c^2 = 16\pi\rho_e r_e$, where $\rho_e$ is the electron density and $r_e$ is the classical electron radius. Therefore, the average mass density of the film is easily determined from the critical wave vector, if the atomic composition of the film is known. The atomic compositions for all the samples as determined by ion beam scattering methods are summarized in Table 1. Examining the SXR curves for the different porogen loadings, it is evident that increasing the porogen content results in a shift of $q_c$ to lower $q$, corresponding to a decrease in the average film density. However, it is not possible to determine the porosity of the films solely from this one measurement.

Exposing the films to saturated toluene vapor leads to capillary condensation of liquid toluene inside accessible pores and a concomitant increase in the density of the films. The difference between critical wave vectors under vacuum and in the saturated toluene is proportional to the toluene uptake into pores and provides a measure of film porosity. The total porosity (P) and the density of wall material separating the pores ($\rho_w$) can be calculated from the relationship: $\rho_{\text{ave}} = \rho_w \times (1 - P)$ and $\rho_{\text{ave,toluene}} = \rho_w \times (1 - P) + \rho_{\text{toluene}} \times P$. Here, $\rho_{\text{ave}}$, $\rho_{\text{ave, toluene}}$, and $\rho_{\text{toluene}}$ are the average density of the film in vacuum, the average density of the film saturated under toluene vapor, and average density of the liquid toluene (0.865 g/cm$^3$ at 20 °C), respectively. One caveat of this method is that it assumes that all pores in the material are filled by toluene; inaccessible pores lead to an underestimate of the porosity and wall density. If the porogen can create inaccessible pores, it then follows that the wall density of the film with greater porogen loading would be less. However, the densities of the wall material for the four films are nearly identical when calculated with this method as shown in Table 1. Thus, the number of inaccessible pores is negligible. Additionally, the porogen architecture does not influence the density of the MSQ matrix.

The porosity of the films increases from approximately 30 to 60% by volume as the porogen loading increases from 20 to 50% by mass. Even when accounting for the estimated densities of the porogens and the MSQ, these porosities are higher than expected. MSQ-type materials generally exhibit intrinsic porosity,[27,28] which can account for this discrepancy. The actual porosity appears to be shifted by an 10% absolute above the porogen loading, suggesting a constant offset due to the micropososity. These results are in good agreement with a previous publication, which indicates approximately 10% porosity in neat MSQ without any porogen. The wall density remains unchanged, (1.464 to 1.482) g/cm$^3$, regardless of porogen loading and porogen architecture. These results also indicate that the efficiency of the porogens at generating porosity is nearly 100%. The detailed structural information of porosity, average film density, and wall density determined for these films are summarized in Table 1.

Despite the similarities in the efficiency of the two porogens, significant differences in the structure of the porous films are evident from the SXR data in Figure 1. Notice that reflectivity curves from TP samples display a broad peak, near $q \approx (4.7 \text{ to } 5.5) \times 10^{-2}$ Å$^{-2}$, indicating an ordered pore

---

(25) Wu, W. L.; Wallace, W. E.; Lin, E. K.; Lynn, G. W.; Glinka, C. J.; Ryan, E. T.; Ho, H. M. *J. Appl. Phys.* **2000**, *87*, 1193.

(26) Parratt, L. G. *Phys. Rev.* **1954**, *95*, 359.

(27) Lee, H. J.; Soles, C. L.; Liu, D. W.; Bauer, B. J.; Lin, E. K.; Wu, W. L.; Gallagher, M. *J. Appl. Phys.* **2006**, *100*, 064104.

(28) Kim, H. C.; Wilds, J. B.; Hinsberg, W. D.; Johnson, L. R.; Volksen, W.; Magbitang, T.; Lee, V. Y.; Hedrick, J. L.; Hawker, C. J.; Miller, R. D. *Chem. Mater.* **2002**, *14*, 4628.

**Table 1. Structural Properties of MSQ-Based Porous Thin Films Prepared from Different Molecular Architecture of Porogen at Varying Loading Contents**[a]

| sample | atomic composition[b] (Si:O:C:H, %) | film density (g/cm$^3$) | wall density (g/cm$^3$) | porosity (%) | average pore diameter (Å) | | |
|---|---|---|---|---|---|---|---|
| | | | | | SANS | XRP | |
| | | | | | | adsorption | desorption |
| NG20 | 25:38:12:25 | 1.042 | 1.482 | 29.7 | 17 | 22 | 26 |
| NG50 | 25:38:12:25 | 0.578 | 1.470 | 60.6 | 80 | 76 | 60 |
| TP20 | 25:38:12:25 | 1.009 | 1.478 | 31.7 | 140[c] | 76 | 30 |
| TP50 | 25:38:12:25 | 0.595 | 1.464 | 59.4 | 158[c] | 132 | 38 |

[a] The relative standard uncertainties of the atomic composition, density, porosity, and pore diameter are ±5%, 0.05 g/cm$^3$, 1%, and 1 Å, respectively. [b] Atomic compositions for samples are provided by IBM Almaden Research Center. [c] Pore diameter of TP sample denotes the distance between pore centers determined from the position of primary Bragg peak. See the details in discussion.

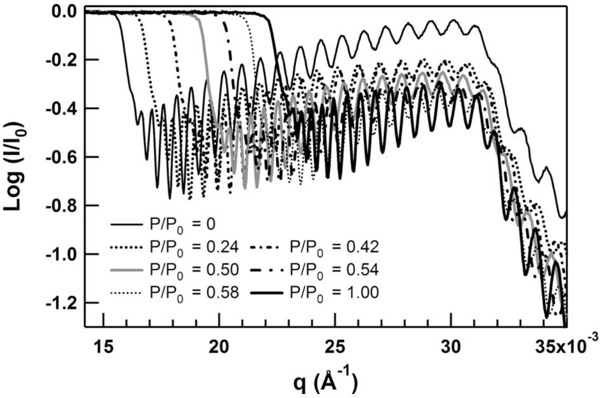

**Figure 2.** SXR curves as increases in the toluene partial pressure for NG50 film. The standard uncertainty in Log ($I/I_0$) is less than the line width.

structure that is absent in the NG samples.[29] The TP porogen acts as an amphiphilic nanoparticle, consisting of a hydrophobic polystyrene (PS) core surrounded by a more hydrophilic copolymer corona of polymethylmethacrylate (PMMA) and polyethyleneglycol (PEG). A consequence of this star architecture is an increase of the osmotic pressure inside the polymer as the concentration in solution is increased.[30,31] This induces an osmotic repulsion, which in turn results in ordering phenomena in thin films from the star shaped nanoparticle.[32,33] Removal of this porogen results in an ordered pore structure in these films through the thickness.

The characteristic length scale between the pores generated by TP can be quantified by the location of the Bragg peak in the reflectivity curve. As the TP porogen concentration increases from 20 to 50% by mass, there is a shift in the Bragg peak to lower $q$ from 0.0545 to 0.0475 Å$^{-1}$, indicating an increase in the characteristic dimensions from 115 to 132 Å. One advantage of star-shaped porogens is their ability to form uniform pore structures without agglomeration. However, this ideal porogen behavior of TP is limited to low loadings. When the concentration of porogen exceeds approximately 30% by volume, the interconnectivity threshold is reached where porogen particles begin to overlap.[27] This phenomenon leads to decreases in degree of order as increases in porosity as evidenced by the less distinct peak in the reflectivity curve of TP50 in comparison to TP20 despite the increase in the number of pores, which alone

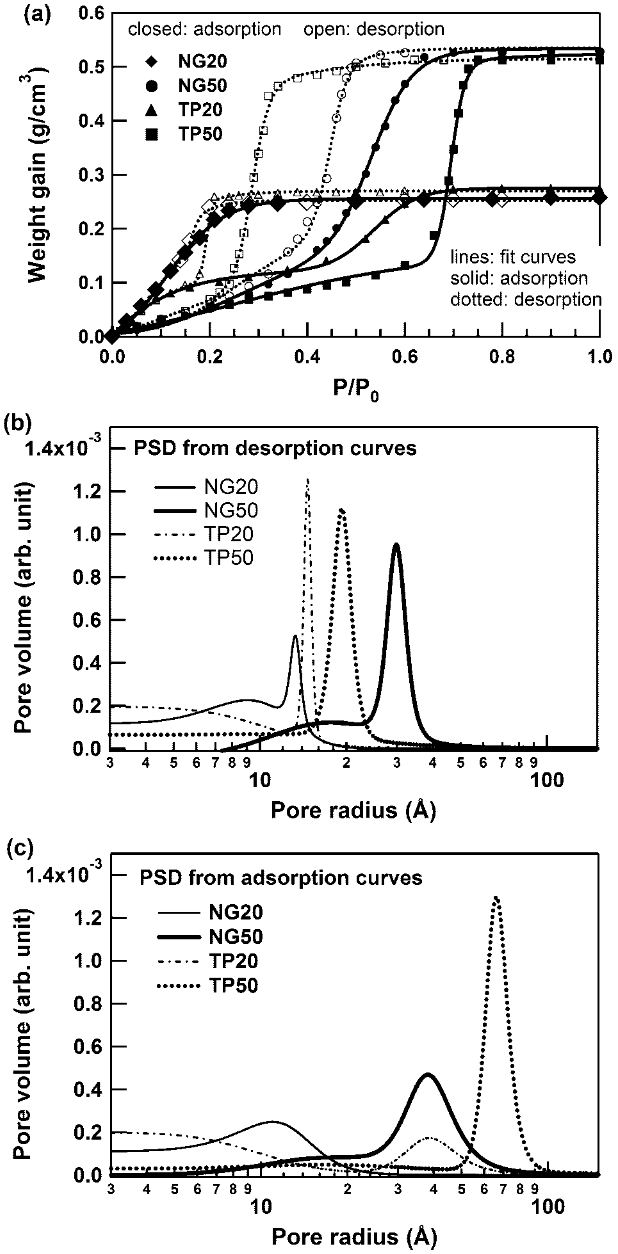

**Figure 3.** (a) Adsorption/desorption isotherms for a series of porous MSQ films formulated with varying loading of porogen and different molecular architecture of porogen. The lines are smooth fits using the sum of a sigmoidal and a log-normal function. (b, c) Pore size distribution from the fits in (a) of the porous MSQ thin films.

---

(29) Vogt, B. D.; Pai, R. A.; Lee, H. J.; Hedden, R. C.; Soles, C. L.; Wu, W. L.; Lin, E. K.; Bauer, B. J.; Watkins, J. J. *Chem. Mater.* **2005**, *17*, 1398.
(30) Birshtein, T. M.; Zhulina, E. B. *Polymer* **1984**, *25*, 1456.
(31) Birshtein, T. M.; Zhulina, E. B.; Borisov, O. V. *Polymer* **1986**, *27*, 1078.
(32) Adam, M.; Fetters, L. J.; Graessley, W. W.; Witten, T. A. *Macromolecules* **1991**, *24*, 2434.
(33) Stancik, C. M.; Pople, J. A.; Trollsas, M.; Lindner, P.; Hedrick, J. H.; Gast, A. P. *Macromolecules* **2003**, *36*, 5765.

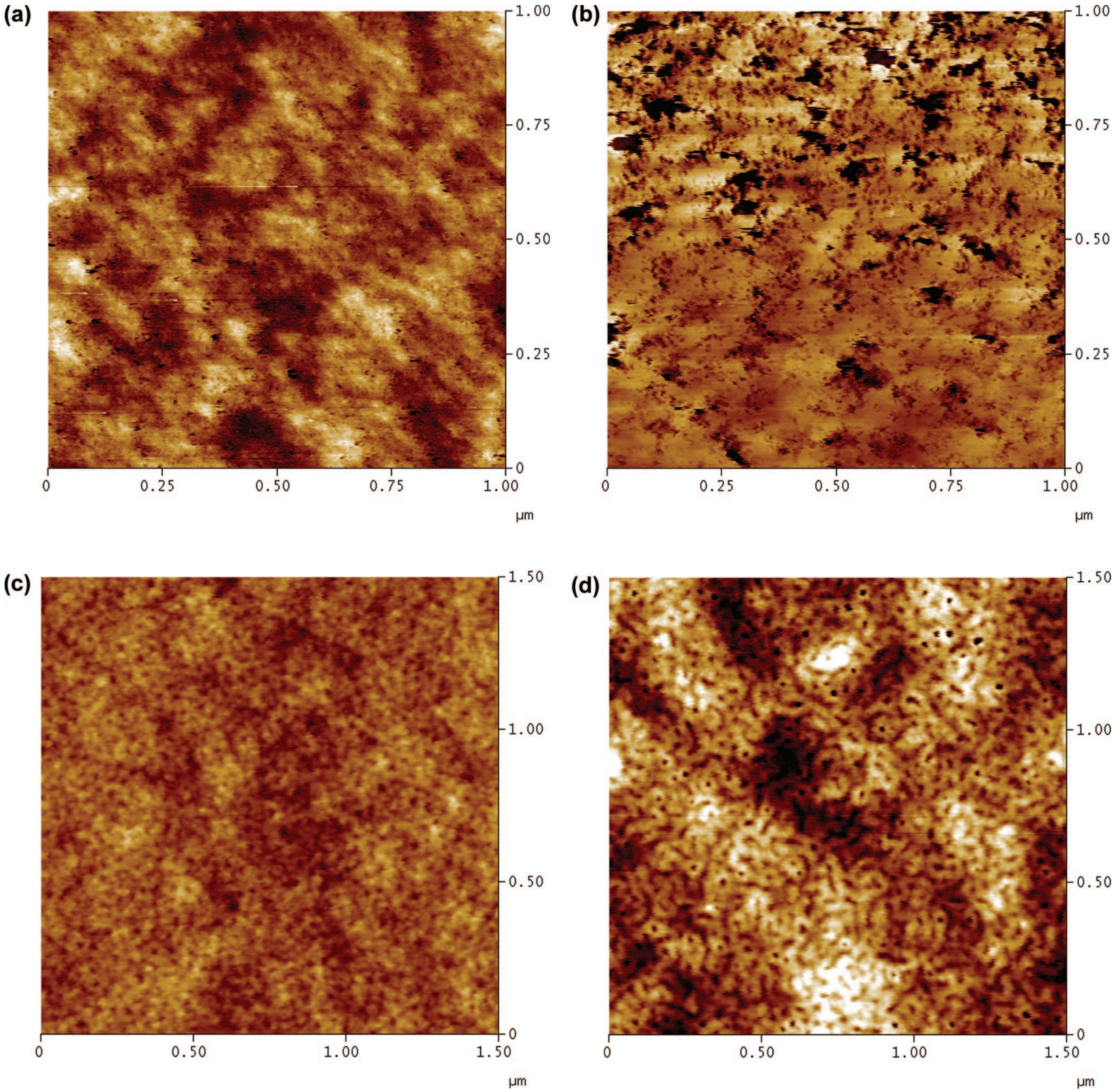

**Figure 4.** AFM micrographs of (a) NG20, (b) NG50, (c) TP20, and (d) TP50 films.

would increase the peak intensity if the ordering remained constant. It should be noted that the order in these materials is still far less than generally observed for cooperative self-assembly of mesoporous film.[34,35]

Adsorption of toluene into the pores decreases the electron density contrast between the pores and wall, resulting in a decrease in intensity of Bragg peak in Figure 1 for the TP samples.[36] Close examination of the TP20 sample reveals a slight shift to lower $q$ or Bragg peak position by approximately 0.001 $Å^{-1}$. This shift corresponds to a dilation in the pore spacing by approximately 2 Å, a 2% increase. We attribute this to a slight swelling of wall material. The thickness of the film can be deduced by the interference (Kessig) fringes in the reflectivity. The periodicity of these fringes also shifts during the adsorption of toluene corresponding to the film swelling by 1%. This swelling is nearly independent of porogen type or loading and therefore attributed to the MSQ matrix. The fact that toluene can slightly swell the matrix suggests that inaccessible pores do not exist. The exposure to saturated toluene vapor allows quantification of the total porosity, but no conclusions can be made regarding the size of the pores for the NG samples as no peaks are present in the reflectivity. Even for the TP samples, quantification of the pore size is limited by assumptions of the space group symmetry to convert the porosity and Bragg peak position to an average pore size.

To ascertain the pore size distribution (PSD) in these films, an analogue of Brunauer−Emmett−Teller (BET) porosimetry is utilized by quantifying the adsorption of toluene as a function of partial pressure with SXR, i.e., XRP. As the

---

(34) Vogt, B. D.; Lee, H. J.; Wu, W. L.; Liu, Y. *J. Phys. Chem. B* **2005**, *109*, 18445.
(35) Ruland, W.; Smarsly, B. *J. Appl. Crystallogr.* **2005**, *38*, 78.
(36) Dourdain, S.; Gibaud, A. *Appl. Phys. Lett.* **2005**, *87*, 223105.

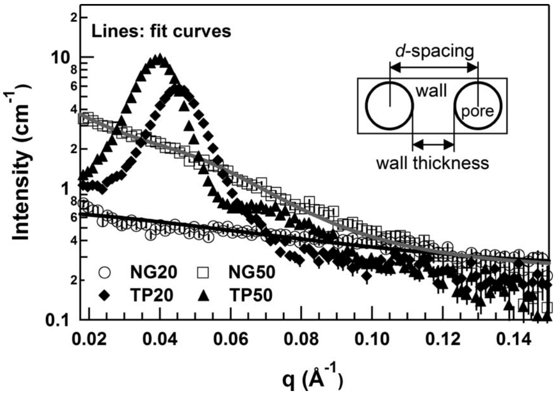

**Figure 5.** SANS data of the porous MSQ films with varying porogen loading contents and different molecular architecture of porogen. Some error bars at the low *q* ranges are within the symbols. NG samples are fit using poly hard sphere model. For TP samples, distances between pore centers or *d*-spacing are determined from the position of primary Bragg peaks. The cartoon in the inset denotes the definitions of *d*-spacing and thickness of wall material separating pores.

toluene partial pressure increases, the maximum pore size that is filled due to capillary condensation also increases. Figure 2 display a series of reflectivity curves collected as a function of toluene partial pressure for the NG50 film. The critical angle shifts to higher $q$ as the partial pressure ($P/P_0$) increases because of the adsorption of solvent vapor inside pores. The shift in the critical angle is directly related to the mass uptake (condensation) of toluene within the film. There is a marked shift in the critical angle near $P/P_0 = 0.5$; this is due to a large population of pores that fill near this partial pressure. As mentioned previously, the sensitivity and resolution of SXR are sufficient to distinguish the subtle changes in the average density of films due to capillary condensation as the atmosphere gradually varies from $P/P_0 = 0$ (air) to $P/P_0 = 1$ (saturated toluene). The mass uptakes induced by toluene adsoprtion in the NG50 film are shown as a function of the relative partial pressure in Figure 3a. Because $q_c$ is proportional to the film electron density, the toluene mass uptake is simply

$$m_{\text{toluene}} = \frac{(\rho_{\text{e,toluene}} - \rho_{\text{e,vac}})M_{\text{toluene}}}{n_{\text{e,toluene}}N_{\text{A}}} \qquad (1)$$

where $M_{\text{toluene}}$ is the molar mass for toluene, $n_{\text{e,toluene}}$ is the total number of electrons in a toluene molecule (50), $N_{\text{A}}$ is Avogadro’s number, and $\rho_{\text{e,toluene}}$ and $\rho_{\text{e,vac}}$ are electron densities of the films in saturated toluene and vacuum environments, respectively. This procedure is repeated for the other three samples examined to determine the toluene uptake as a function of $P/P_0$ as illustrated in Figure 3a.

The adsorption and desorption isotherms display several features that are related to the porosity and PSD. The toluene uptake in all cases initially increases at low $P/P_0$ because of to filling of the smallest micropores that are intrinsic to the MSQ material. For all samples except the NG20, there is a second dominant uptake at intermediate partial pressures, indicating a second population of larger mesopores. This second uptake shifts to larger $P/P_0$ in the order of NG50, TP20, and TP50, indicating a corresponding increase in the average pore radius for this second population of pores. Finally, the mass uptake plateaus at high partial pressure when all the pores are completely filled. The amplitude of this plateau is proportional to the total porosity and there does not appear to be a dependence of the total porosity on the porogen type (NG vs TP). However, the details of the pore structure vary significantly with both porogen architecture and loading. For the NG samples in the low partial pressure regime, notice that the initial uptake of toluene decreases as the porogen loading increases from 20 to 50 % by mass. This indication of reduced microporosity with the addition of porogen is consistent with the micropores being intrinsic to the matrix material. As the porogen loading increases, the volume fraction of matrix material will decrease. However, the total porosity increases with the addition of the larger mesopores. The same basic trend is observed with the TP sample: fewer small pores with the addition of porogen.

As the partial pressure increases during the adsorption branch of the isotherm, solvent molecules progressively condense into larger and larger pores. However, during desorption the egress of toluene from the larger pores can only occur through the surrounding smaller pores. This means that the larger pores are not free to desorb at the relative pressure corresponding to their critical capillary radius because the smaller blocking pores are filled with the condensed adsorbate. The manner by which these smaller pores block the desorption of the larger pores is referred to as the “ink bottle effect”. The result is a simultaneous draining of both the small and large mesopores at a partial pressure corresponding to the critical radius of the smaller pores. Differences between the adsorption and desporption isotherms contain information about the interconnectivity between the pores and the PSD.[37,38] Therefore, in the case of pore blocking, the evaporation occurs at the equilibrium pressure of the meniscus in the pore neck, and information about the neck size can be obtained from the desorption branch of the isotherm.

As the porogen loading of the NG sample increases from 20 to 50% by mass, an appreciable hysteresis loop develops, suggesting the onset of interconnected mesopores. Compared to NG50, the hysteresis loop of TP50 is considerably wide and the slopes of isotherms are fairly steep. This wide loop suggests that mesopores are connected through smaller interconnecting pores. A steep slope indicates narrower distribution of pore sizes in the TP50 sample due to a greater propensity to form isolated mesopores. Additionally, TP20 has a noticeable hysteresis loop indicative of mesopores.

These qualitative descriptions of the adsorption/desorption isotherms in Figure 3a can be made quantitative by invoking models to fit the data. Most of these models start with the Kelvin equation for capillary condensation that relates the partial pressure to a pore radius. By modeling both the adsorption and desorption branches, one can obtain quantitative PSDs and neck radii for the pores or channels connecting the pores. However, the models must be highly complicated to account for the energetic interactions of the probe models and the pore surface, the geometry of the pores and necks

---

(37) Kruk, M.; Jaroniec, M. *Chem. Mater.* **2001**, *13*, 3169.
(38) Kraemer, E. O. *A Treatise on Physical Chemistry*; Taylor, H. S., Ed.; Macmillan: New York, 1931; p 1661.

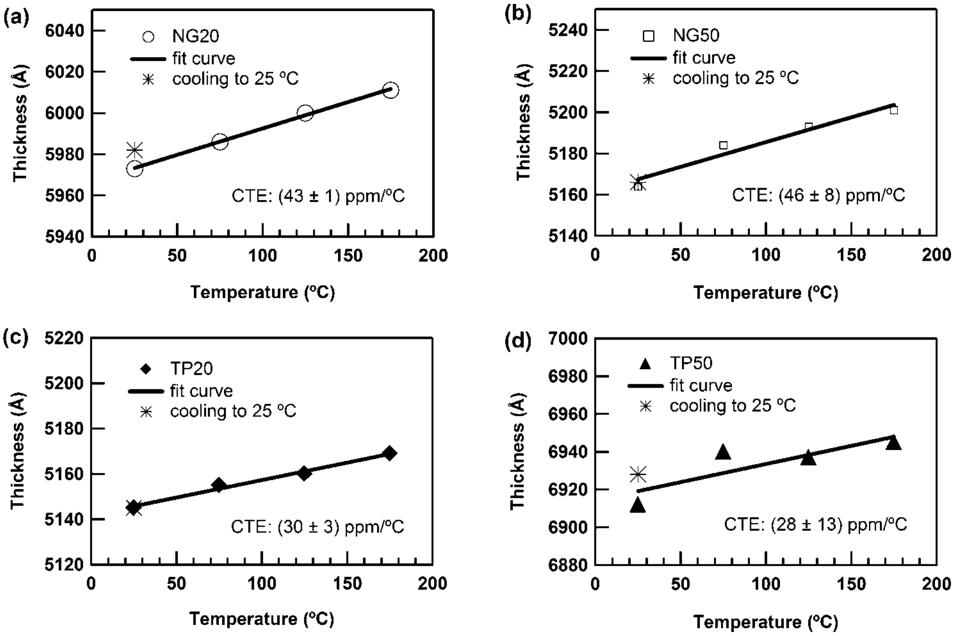

**Figure 6.** Thickness changes as the temperature varies from 25 to 175 °C: (a) NG20, (b) NG50, (c) TP20, and (d) TP50. The coefficient of thermal expansion for each porous sample is recorded in the figures.

(cylindrical, spherical, and irregular), and even possible chances in the nature of the liquid (vapor−liquid coexistence) in the pore. Given that our pores are far from being ideal channels or spheres with well understood wetting behaviors, we will take a highly simplified approach here and model the isotherms with the basic Kelvin equation as a first approximation. Rather than try to determine which modification to the Kelvin equation is most appropriate, we turn to an independent scattering technique (SANS) to evaluate the physicality of PSDs from this simplified approximation.

The Kelvin equation offers the simplest relation between $P/P_0$ and the critical pore size ($r_c$) for capillary condensation

$$r_c = -\frac{2V_m\gamma}{RT}\frac{1}{\ln(P/P_0)} \qquad (2)$$

where $\gamma$ is the liquid surface tension, $V_m$ is the molar volume of the liquid, $P$ is the vapor pressure, and $P_0$ is the equilibrium vapor pressure at temperature $T$. There are alternative models to the Kelvin equation for quantifying $r_c$ from the partial pressure (see refs 27 and 29). Regardless, the Kelvin equation provides a simple, yet powerful way to quantify PSDs from the isotherms in Figure 3a. Panels b and c in Figure 3 show the PSDs from the desorption and adsorption isotherms, respectively.

Generally, there is a tremendous difference in the PSDs calculated from the adsorption and desorption isotherms. This is the “ink bottle effect” resulting from interconnected mesopores.[37,39] It is generally believed that the PSD from desorption branch reflects the constricting diameters of the neck between the larger pore domains. The desorption peaks are centered at approximately 13, 30, 15, and 19 Å for NG20, NG50, TP20, and TP50, respectively. The disordered pores from the NG porogen exhibits a larger increase in the size of interconnecting pores when the porogen loading is increased, compared to a subtle increase for the TP porogen at similar loading. Besides the sharp peak in the PSDs due to the porogen, there is also a broad feature at smaller pore sizes reflecting native microporosity of the MSQ. Note that the microporosity decreases as the porogen loading increases as less MSQ is present.

The PSD obtained from the adsorption isotherm is less sensitive to minimum constricting diameter of the interconnected domains, giving a better picture of the larger pores. There are no interdependencies on pore filling because there is not the draining of the interconnected mesopores. The linear porogen (NG) at 20% by mass in the MSQ yields broad microporosity peak centered at approximately 11 Å (Figure 3c) with the largest pores having a radius of nearly 20 Å. Increasing the NG concentration to 50% eliminates a significant fraction of the micropores (<10 Å) and shifts the peak center to nearly 40 Å. There is a shoulder at lower pore sizes covering the range from approximately 10 to 25 Å. Interestingly the peak location for NG50 is similar to TP20. The star polymer porogen is intrinsically larger than the NG porogen leading to a larger average pore size at comparable porogen contents. There is almost a bimodal distribution of pores in TP20 with distinct peak centered at 38 Å and then a broader distribution of micropores extending up to approximately 20 Å. This distribution can be explained by the intrinsic porosity of the MSQ leading to the broad micropore size distribution with the self-assembled TP porogen responsible for the peak near 38 Å. Increasing the concentration of the TP to 50% decreases the microporosity and shifts the peak in the PSD to larger pores. A similar shift to larger pores is seen when increasing NG porogen concentration. Table 1 summarizes the approximate positions for the dominant peaks in the different samples.

In general, the average pore size increases with increased porogen loadings. However, the average pore size produced

---

(39) Sing, K. S. W.; Everett, D. H.; Haul, R. A. W.; Moscou, L.; Pierotti, R. A.; Rouquerol, J.; Siemieniewska, T. *Pure Appl. Chem.* **1985**, *57*, 603.

by the porogen is dependent upon the porogen architecture. The NG porogen leads to aggregates with increased loading, more than tripling the average pore size as the porogen loading increases from 20 to 50% by mass (22 Å to 76 Å in diameter). In comparison, the TP porogen exhibits less aggregation between porogen leading to a smaller fractional increase in the average pore size for the same porogen loading range (76 to 132 Å in diameter). Less aggregation of star-shaped porogen is evidenced by the fact that the average pore size of TP20 is identical to the hydrodynamic radius ($R_h$) of porogen determined in tetrahydrofuran (THF) by dynamic light scattering, 78 Å.[20] Comparison of TP50 and NG50 illustrate a significant difference between the pores generated by these different porogens. There is a significant shoulder to the peak in the PSD in NG50, whereas TP50 does not show this shoulder and instead exhibits a small fraction of pores whose population is nearly constant up to a radius of 25 Å.

We can attribute these differences in the calculated PSDs to the aggregation behavior of the porogens and its influence on the film morphology. The interpretation of the film morphology from the porosimetry measurements can be contrasted with the surface topology imaged by atomic force microscopy (AFM), which characterizes a small area of the local film structure as shown in Figure 4. The NG sample displays a random (and broad) size distribution of pores from the micrograph. The largest pores tend to be connected to smaller pores, presumably these smaller pores act to interconnect the large pores as suggested by the porosimetry data. The TP sample shows a relatively uniform size distribution and some degree of local ordered. This isolated uniform structure is not only consistent with the porosimetry results, but also with the Bragg peak observed in the reflectivity data.

SANS measurements were also performed for a direct measure of the thin film morphology and providing an ensemble average of the nanoscale morphology. The average pore size determined from SANS can be used to compare to the XRP data presented previously. Figure 5 displays the SANS intensity from the samples under vacuum as a function of $q$, where $q = (4\pi/\lambda)\sin(\theta/2)$ and $\theta$ is the scattering angle. The scattering arises from differences in the neutron scattering length density of connecting wall material and the pores. Larger pores result in stronger scattering at lower $q$. Because the scattering intensity is proportional to the number of scattering objects, such as pores, the samples with larger porogen loadings are expected to scatter more just on the basis of an increase in the number of pores. Comparing the different scattering profiles, it is clear that the pore structure from TP and NG porogens are extremely different.

There is a strong scattering maximum for TP20 and TP50 centered at 0.046 and 0.040 $\text{Å}^{-1}$, respectively with a broad shoulder at slightly higher $q$ values. This scattering profile is similar to the one obtained from a surfactant templated mesoporous silicate where the peak is associated with the mesopores, while the shoulder is attributed to micropores.[29] SANS has been often utilized to investigate for ordering of this star shaped polymer previously.[40–45] Although the scattering from the TP based samples is not suitable for classic crystallographic methods where the scattering is given by a superposition of the structure and form factors, the primary scattering maxima defines the $d$-spacing ($l$) of locally ordered pores by $l = 2\pi/q^*$, where $q^*$ is the location of the scattering maxima.[46] Here, $d$-spacing denotes the average distance between mesopore centers (inset in Figure 5). The $d$-spacing of TP20 and TP50 is 140 Å and 158 Å, respectively. Combining this result with the average pore size determined from XRP, the thickness of wall material separating pores can be estimated to be 64 and 26 Å for TP20 and TP50, respectively.

Scattering data of the NG samples show a smooth decay in intensity without any peaks, consistent with randomly distributed pores. The SANS data are analyzed using the "poly hard sphere" model to extract an average pore size.[47] This function calculates the scattered intensity for a population of polydisperse spheres, which includes hard sphere interactions between the particles. The calculation is an exact, multicomponent solution, using Percus−Yevick closure. A Schulz distribution is used to describe the polydispersity of the sphere diameter. However, the volume fraction (or porosity) and scattering contrast are correlated, thus the porosity determined from XRP is used during model fitting. Fits for NG20 and NG50 yield an average pore diameter of 17 and 80 Å, respectively; these values are in good agreement with the average pore size calculated from the adsorption isotherm. Capillary porosimetry techniques are widely used in the semiconductor industry [48,49] because the general shape of the adsorption/desorption isotherms provide valuable insights into the pore structure. These results confirm the utility of this method to characterize the pore morphology with good agreement between the porosimetry, SANS, and AFM measurements.

For low-$k$ dielectric integration the coefficient of thermal expansion (CTE) of the dielectric material is a key factor to be considered; to minimize the thermal stress incurred in the system during processing it is necessary to reduce the differences in CTE between silicon and the low-$k$ material. The film thickness is determined using SXR with a subnanometer resolution at temperatures from 25 to 175 °C under a vacuum as illustrated in Figure 6. To rule out the possibility of any undesirable thermal induced structure changes includ-

---

(40) Likos, C. N.; Löwen, H.; Watzlawek, M.; Abbas, B.; Jucknischke, O.; Allgaier, D. *Phys. Rev. Lett.* **1998**, 8–4450.

(41) Likos, C. N.; Löwen, H.; Poppe, A.; Willner, L.; Roovers, J.; Cubitt, B.; Richter, D. *Phys. Rev. E* **1998**, *58*, 6299.

(42) Marques, C. M.; Izzo, D.; Charitat, T.; Mendes, E. *Eur. Phys. J. B* **1998**, *3*, 353.

(43) Willner, L.; Jucknischke, O.; Richter, D.; Farago, B.; Fetters, L. J.; Huang, J. S. *Europhys. Lett.* **1992**, *19*, 297.

(44) Dozier, W. D.; Huang, J. S.; Fetters, L. J. *Macromolecules* **1991**, *24*, 2810.

(45) Richter, D.; Jucknischke, O.; Willner, L.; Fetters, L. J.; Lin, M.; Huang, J. S.; Roovers, J.; Toporocski, C.; Zhou, L. L. *J. Phys. IV* **1993**, *3*, 3.

(46) Polarz, S.; Antonietti, M. *Chem. Commun.* **2002**, 2593.

(47) Griffith, W. L.; Triolo, R.; Compere, A. L. *Phys. Rev. A* **1987**, *35*, 2200.

(48) Grill, A.; Patel, V.; Rodbell, K. P.; Huang, E.; Baklanov, M. R.; Mogilnikov, K. P.; Toney, M.; Kim, H.-C. *J. Appl. Phys.* **2003**, *94*, 3427.

(49) Baklanov, M. R.; Mogilnikov, K. P. *Microelectron. Eng.* **2002**, *64*, 335.

ing pore collapse or material degradation, the film thickness of each sample is measured after cooling back to 25 °C. This second measurement at 25 °C always coincides with the value determined at the first measurement, so the porous film does not appear to change during the CTE measurements.

The film thickness can be obtained by modeling the SXR data in terms of a least-squares fitting based on the Parratt algorithm[26] as mentioned earlier. However, when the thin film consists multiple layers with complex depth dependent electron density, it is not always possible to achieve a reliable fit to extract the film thickness due to the large number of the fitting parameters involved. We have developed an algorithm to extract film thickness information without fitting the entire reflectivity curve. The procedure to extract film thickness from the SXR results is outlined as follows. At angles greater than the critical angle of silicon, the oscillation in the SXR data is due to the interference of radiation reflected from the air/film and film/silicon interfaces. However, in the region close to the critical angle of silicon, the simple relation between film thickness and the periodicity of the interference fringes is not strictly true due to dynamical scattering effects. The film thickness is thus best determined from the spacing or the periodicity of the fringes in the high $q$ region. In this work, the high $q$ regime is defined as the $q$ range where the log $(I/I_0)$ lies below $10^{-2}$. In this regime, multiple scattering constitutes less than 1% of the reflected intensity.[25] After selecting a suitable $q$ range showing the periodic constructive/destructive interference fringes, SXR intensities are plotted as a function of $q'$ defined as $(q - q_c^2)^{1/2}$, where $q_c$ is the magnitude of critical wave vector of thin film. The $I(q')$ data are Fourier filtered to remove both the high and low frequency noises. The baseline of the filtered $I(q')$ data is then flattened by multiplying the SXR intensity by $(q')$.[4] The peak position of the filtered and flattened data is collected with a simple algorithm. From the peak position and the order of the peak the average spacing $\Delta q'$ between adjacent peaks is determined and the film thickness is calculated as $d = 2\pi/\Delta q'$. As shown in Figure 6, the CTE of the NG samples is approximately 1.5 times larger than for the TP samples as we expected. These CTE results illustrate another important property that can potentially be tuned through the porogen architecture. The CTE is independent of the porogen contents. The CTE determined for all four films, which is less than most amphorous polymers, but still slightly larger than silicon.

## Conclusions

The influence of porogen architecture and loading on the structural characteristics of MSQ based porous films was studied with a combination of XRP, SANS, and AFM. The MSQ wall density of the material between the pores is unaffected by the choice of porogen or its concentration. Similarly the CTE is not influenced by the porogen loading; however, the samples prepared with the linear polymer porogen exhibit a CTE approximately 50% greater than those made with a star polymer porogen. Minimizing the CTE is one key factor in the choice of low-*k* material for integration. Both porogens generate porosity with nearly 100% efficiency. However the morphology and PSD is strongly dependent upon the molecular architecture of the porogen. The linear polymer porogen yields porous films with a broad size distribution of disordered pores, whereas use of the star polymer porogen results in an ordered porous structure with a more uniform pore size. The ordering of this porogen is due to the amphiphilic nature of the star polymer. For both porogens, increasing the loading results in an increased pore size; however, the extent of pore size change is much greater for the linear polymer porogen. This linear porogen at high loading (50%) generates a broad distribution of large (≈ 4 nm radius) pores; however at 20% porogen loading, the resultant film contains small isolated pores (all pores <2 nm) that would be appropriate as a low-*k* dielectric for microelectronics. Conversely, the star porogen generates an ordered pore structure that is too large for integration as low-*k* dielectric, but is suitable for bioseparation applications. Thus, the porogen architecture plays a vital role in determining the pore structure and ultimately the utility of the porous material for the desired application.

**Acknowledgment.** This research was financially supported by the National Institute of Standards and Technology (NIST) Office of Microelectronic Program. Access to the neutron scattering facilities was made available through the NIST Center for Neutron Research. The authors are also grateful for the technical assistance with the neutron scattering measurements from Derek Ho and Charles Glinka.

CM800872B